Absorption line metrology by optical feedback frequency-stabilized cavity ring-down spectroscopy

Johannes Burkart · Samir Kassi

Abstract Optical feedback frequency-stabilized cavity ring-down spectroscopy (OFFS-CRDS) is a near-shot-noise-limited technique combining a sensitivity of 2×10^{-13} cm$^{-1}/\sqrt{\text{Hz}}$ with a highly linear frequency axis and sub-kHz resolution. Here, we give an in-depth review of the key elements of the experimental setup encompassing a highly stable V-shaped reference cavity, an integrated Mach-Zehnder modulator and a tightly locked ring-down cavity with a finesse of 450,000. Carrying out a detailed analysis of the spectrometer performance and its limitations, we revisit the photo-electron shot-noise limit in CRDS and discuss the impact of optical fringes. We demonstrate different active schemes for fringe cancelation by varying the phase of parasitic reflections. The proof-of-principle experiments reported here include a broadband high-resolution spectrum of carbon dioxide at 1.6 μm and an isolated line-shape measurement with a signal-to-noise ratio of 80,000. Beyond laboratory-based absorption line metrology for fundamental research, OFFS-CRDS holds a considerable potential for field laser measurements of trace gas concentrations and isotopic ratios by virtue of its small sample volume and footprint, the robust cavity-locking scheme and supreme precision.

1 Introduction

Ultra-sensitive measurements of molecular absorption by means of continuous-wave-laser cavity ring-down spectroscopy (CW-CRDS) [1] have a multitude of applications in atmospheric trace gas concentration monitoring and the detection of extremely weak absorption features [2] for improving spectroscopic databases [3–5]. In recent years, the increasing demand for precision field measurements is reflected by a growing market for commercial CRDS field instruments [6] detecting various relevant molecules in situ at atmospheric concentrations. This process is accelerated by the rapidly developing field of spectroscopic isotopic ratio measurements [7], whose long-term objective is replacing bulky and expensive dual-inlet isotopic ratio mass spectrometers by compact, inexpensive and highly selective near- or mid-infrared laser instruments. Significant progress in measuring the isotopic anomalies of ^{2}H, ^{17}O, ^{18}O and ^{13}C has been made for important atmospheric constituents such as water vapor [8, 9], carbon dioxide [10] and methane [11], equally triggering the development of commercial devices [12].

In CRDS, the absorption coefficient α of a gas sample filling an optical cavity is obtained from a measurement of the exponential ring-down (RD) decay time τ via

$$\alpha c = \tau^{-1} - \tau_0^{-1} \tag{1}$$

c being the speed of light and τ_0 the RD time on the spectral baseline. Relying purely on time and frequency measurements, CRDS holds the promise of highly accurate, SI-traceable line strength measurements for validating *ab initio* calculations [13, 14], which could pave the way to absolute gas concentration measurements by laser spectroscopy [15]. Besides high sensitivity, a stable and linear

J. Burkart (✉) · S. Kassi
Univ. Grenoble Alpes, LIPhy, 38000 Grenoble, France
e-mail: johannes.burkart@ujf-grenoble.fr

J. Burkart · S. Kassi
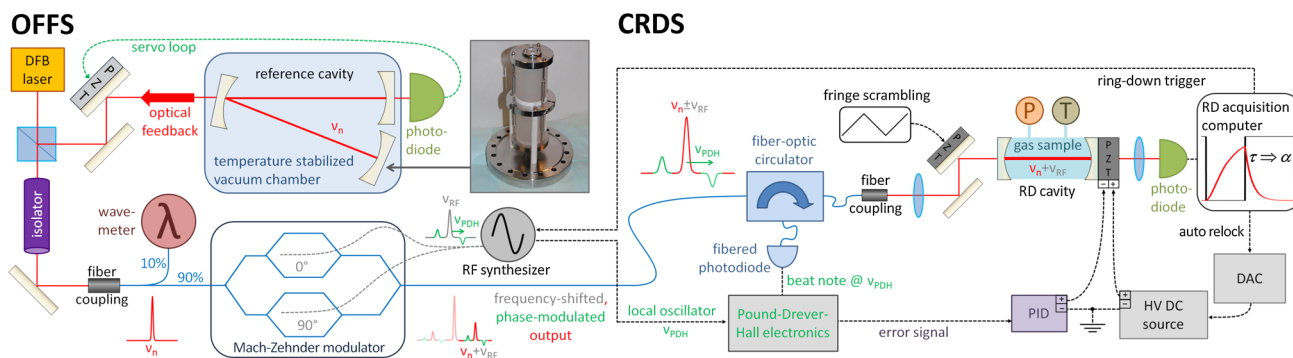CNRS, LIPhy, 38000 Grenoble, France

Fig. 1 Schematic of the experimental setup for optical feedback frequency-stabilized cavity ring-down spectroscopy (OFFS-CRDS)

frequency axis is vital for such precision measurements. This issue has been addressed by frequency-stabilized CRDS (FS-CRDS) [16, 17], which consists in locking the laser to a dichroic-mirror RD cavity stabilized by means of a helium-neon laser. The advent of FS-CRDS has fostered experimental development for high-fidelity line-shape measurements beyond the Voigt profile [18, 19], crucial for an accurate retrieval of line parameters and a physical understanding of intermolecular potentials and collision processes [20–22].

The recently developed optical feedback frequency-stabilized cavity ring-down spectroscopy (OFFS-CRDS) technique [23] follows a distinctly different route to CRDS frequency stabilization. It is based on tightly locking a high-finesse ring-down cavity on a narrow laser referenced to a highly stable resonator via a tunable radio frequency. Combining extreme sensitivity with an undistorted frequency axis, the method was conceived to address current and future challenges in high resolution and sensitivity molecular spectroscopy. It exhibits performances suitable for fundamental applications, such as an optical determination of the Boltzmann constant [24–26], as well as both robustness and limited complexity compatible with field measurements in demanding environments [27–29].

2 Method and experimental setup

In particular, OFFS-CRDS was designed to meet the following five intimately related requirements: (1) a sensitivity on a par with state-of-the-art CW-CRDS setups, (2) a highly stable and linear frequency axis, (3) the absence of excess absorption noise due to frequency jitter conversion on slopes, (4) an arbitrary frequency stepping resolution for resolving delicate features of advanced Doppler-broadened line shapes or even sub-Doppler features, and, in turn, (5) very high intracavity power for saturating even weak transitions in the near infrared. (1) and (5) call for the resonant excitation of a very high-finesse cavity which guarantees

long, well-defined RD events and strong passive intra-cavity power amplification. (2) and (3) necessitate a highly stable optical length of the RD cavity, while (4) combined with (2) suggests working in the radio frequency (RF) domain, where sub-Hz frequency accuracy and resolution are readily achievable.

Fulfilling all five conditions, our approach consists in tightly locking a high-finesse RD cavity to a sub-kHz linewidth stable laser finely tunable by means of electro-optic single-sideband modulation. Among the key elements of this setup are the optical feedback frequency-stabilized laser using a highly stable V-shaped reference cavity and single-sideband modulation with a dual-parallel Mach-Zehnder modulator (MZM) [30], as well as a modified fibered Pound-Drever-Hall-locking scheme for tight locking of a high-finesse RD cavity [23]. These methodological advances provide high cavity transmission for low-noise photodetection and guarantee an unbroken stability transfer chain from the V-shaped reference cavity to the absorption spectrum frequency axis. An overview of the experimental setup for OFFS-CRDS is depicted in Fig. 1.

2.1 Optical feedback frequency stabilization and single-sideband modulation

A distributed-feedback (DFB) diode laser emitting between 1,608 and 1,616 nm is locked to a high-finesse V-shaped Fabry-Pérot cavity by optical feedback. The optical self-locking of diode lasers to an external feedback cavity [31, 32] relies on the stable frequency and phase of the resonant light field in the feedback cavity. When its backward transmission is reinjected into the laser medium, the stimulated emission by feedback photons counteracts the random walk of laser phase due to spontaneous emission. This leads to laser linewidth narrowing by several orders of magnitude and frequency locking to feedback cavity resonance. The optical-feedback-locking range is proportional to the square root of feedback power [32]. We therefore use a Glan-Taylor polarizing beam splitter to divert a

percent-level fraction of the total laser power toward the V-cavity. The feedback power is fine-tuned for obtaining a locking range equal to the free spectral range (FSR) between successive longitudinal modes of the cavity. The light not needed for optical feedback locking is coupled into a polarization-maintaining (PM) optical fiber carrying roughly 50 % of the initial laser power. As the relative phase of the feedback field gives rise to frequency pulling within the cavity modewidth, a sub-kHz-bandwidth servo-loop actively controlling the laser-cavity distance is needed to keep the laser locked to the center of a TEM_{00} resonance. The corresponding error signal is obtained by laser current modulation at a few kHz and phase-sensitive first-harmonic detection in cavity transmission.

The highly stable reference cavity [30] consists of a vertically mid-plane mounted 15-cm-long cylindrical ultra-low expansion (ULE) glass spacer with Super Invar mirror holders tightly contacted to both ends. These cavity flanges are precision-machined for holding three dielectric mirrors at appropriate angles for automatic and permanent V-shape alignment. The reference cavity is placed in a high-vacuum chamber pumped down to a few 10^{-7} mbar. The latter is temperature stabilized to better than 8 mK over its entire surface.

This optical feedback frequency-stabilized laser source features a linewidth below 530 Hz at 1 s and drift rates below 20 Hz/s. The laser locks to successive reference cavity modes when its current or diode temperature are changed, thereby enabling easy and fast mode-by-mode frequency tuning over 8 nm.

To cover the spectral gap between reference cavity modes, we have proposed fine-tuning by single-sideband modulation using a PM-fiber-coupled dual-parallel Mach-Zehnder modulator (MZM) [30, 33]. In its nested lithium niobate $LiNbO_3$ interferometer waveguide, phase-modulation sidebands generated via the electro-optic Pockels effect undergo DC-voltage-controlled destructive and constructive interferences yielding a single-sideband output. The optical carrier is suppressed by static destructive interference in the two inner Mach-Zehnder interferometers (cf. Fig. 1). The suppression ratios of unwanted spectral components are better than 28 dB [30]. The accuracy and resolution of this frequency-shifting mechanism are given by the RF synthesizer (Rohde&Schwarz SMB100A) referenced to a 10 MHz Rubidium timebase (SRS PRS10). The tuning range of the present setup was limited to approximately 1 GHz by the bandwidth of the 90° hybrid coupler (Mini-Circuits ZX10Q-2-19+) needed for driving the two RF electrodes of the MZM (Covega Mach-10-060). In a follow-up setup currently under preparation, a commercial 2–18 GHz broadband hybrid coupler will be used for achieving a 32-GHz tuning span around the optical feedback frequency-stabilized carrier.

Summing up, the optical frequency ν synthesized by the single-sideband-tuned optical feedback frequency-stabilized laser is

$$\nu = \nu_0 + k \times \text{FSR} \pm \nu_{\text{RF}} \tag{2}$$

where k is the number of the V-cavity mode the laser is locked to and ν_0 is the optical frequency of the arbitrarily chosen mode defined as $k = 0$. ν_0 and k are measured by monitoring ten percent of the optical feedback locked laser power on a Fourier-type wavemeter (Burleigh WA-1650). According to Eq. (2), this procedure limits the knowledge of ν to the wavemeter accuracy of ±20 MHz. This limitation could be readily overcome by monitoring the beat note of the stable laser with a self-referenced frequency comb [34]. The uncertainty of the MZM-generated frequency shift $\pm\nu_{\text{RF}}$ is well below the Hz-level.

In view of Eq. (2), it is also essential to have a precise knowledge of the V-cavity FSR and its slight wavelength-dependence in order to record spectra by using its modes as a frequency grid. A precision measurement of this quantity was carried out by successively locking the laser to two distant modes of the V-cavity and recording its beat note with a self-referenced frequency comb (Toptica FFS1550) using a 200 MHz 16-bit acquisition card (GAGE model CS1622). Using a less precise value for the FSR from previous wavemeter-based measurements, the two V-cavity modes could be unambiguously numbered and the beat notes combined to yield an accurate measurement of their frequency spacing. Dividing it by the number of modes yields the Hz-level precision average FSR values for different laser wavelength intervals shown in Fig. 2. The linear trend at the limit of statistical significance can be attributed to mirror dispersion. For most applications, using the weighted average $\overline{\text{FSR}} = 491,395,463(6)$ Hz over the entire spectral interval is sufficient in Eq. (2). Knowing the FSR, the V-shaped cavity finesse around 2.8×10^5 was determined by means of a ring-down measurement [35]. In the absence of technical noise, this would correspond to a sub-Hz laser linewidth under optical feedback locking [32].

2.2 Pound-Drever-Hall cavity-locking and ring-down measurement

The RD cavity used here consists of two highly reflective dielectric mirrors separated by a massive 33-cm-long aluminum hollow cylinder of 50 mm outer and 8 mm inner diameter with a lateral 1/4″-NPT vacuum fitting for pumping and gas inlet. The cavity output mirror mounted on a piezo-electric actuator (PZT) allows tuning the TEM_{00} mode of the cavity to resonance with the stable laser. This necessitates a relative voltage stability on the order of the inverse cavity finesse, which ranges from 425,500 at 1,616 nm to 462,200 at 1,608.5 nm here. For achieving

Fig. 2 Measured average reference cavity free spectral range for different laser wavelength intervals
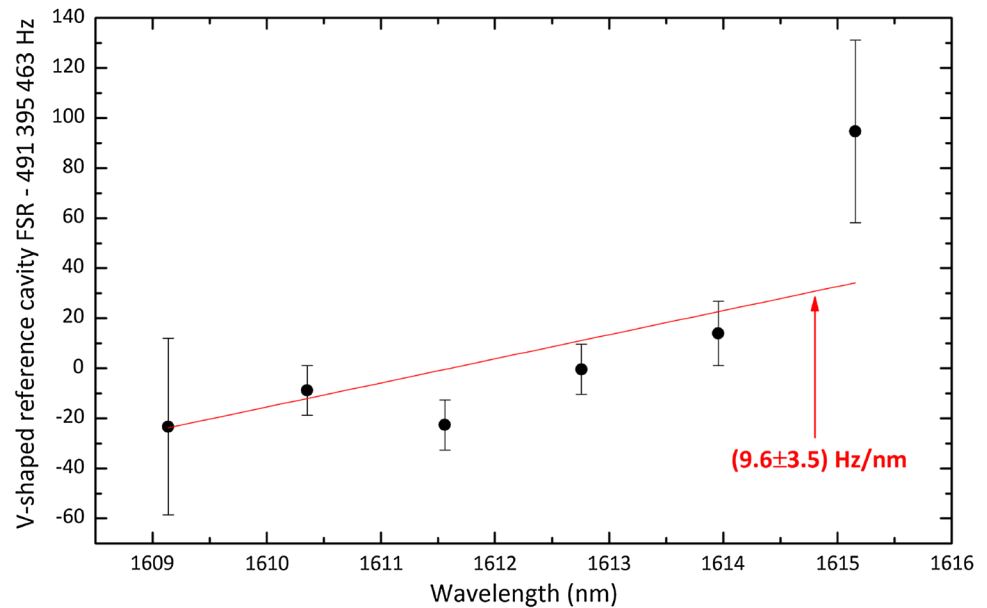
this challenging stability goal, we realized the split voltage supply scheme illustrated in Fig. 1. The PZT electrodes are driven by two signals referenced to a common ground, one low-noise, low-bandwidth high-voltage component and one 7 kHz-bandwidth low-voltage signal from a commercial analog servo controller (Toptica PID110). This approach allows for a two-step automated relock procedure discussed in detail in Sect. 2.3.

To obtain an error signal for the analog servo loop, we set up an all-fibered, slightly modified Pound-Drever-Hall (PDH) locking scheme [36]. In PDH locking, a phase-modulation sideband pair serves as a phase- and frequency detector for the optical carrier in cavity reflection. Instead of adding an electro-optic modulator for generating these sidebands, we supply a phase-modulated RF at the MZM input, which generates a single-sideband frequency-shifted optical signal with small phase-modulation satellites. The resulting PDH signal in cavity reflection is detected on a fibered photodiode (PD) by means of a fiber-optic circulator. This robust locking scheme reduces experimental complexity and minimizes insertion losses. The RF driving the MZM is phase-modulated at $\nu_{PDH} = 400$ kHz and the error signal retrieved with commercial general-purpose RF components, such as bandpass filters (Mini-Circuits ZFBP-400K+) and amplifiers (Mini-Circuits ZFL-500LN+).

As soon as a certain cavity transmission threshold is reached, RD events are triggered by a 5-V TTL (transistor-transistor logic) signal driving a broadband absorptive RF switch (Minicircuits ZASWA-2-50DR+). The switch cuts the MZM single-sideband output by attenuating the RF driving signal by more than 80 dB within tens of nanoseconds. In this scheme, contrary to classical CW-CRDS, an acousto-optic modulator with additional insertion losses and inferior

switching characteristics is no longer needed. The RD signals on the transmission PD are acquired at a sampling rate of 650 kHz by an 18-bit analog-to-digital converter (ADC) card (NI PCI-6281). Figure 3 shows an example of a PDH-locked RD measurement with an acquisition time of 1.2 ms per RD, resulting in a RD event rate of approximately 400 Hz. As the robust locking is not perturbed by the RD events, switching the light back on leads to near-exponential transmission ring-up events, which exhibit random intensity noise features mainly due to residual frequency jitter at the sub-kHz level. Exponential least-squares fitting of the RD signals is carried out in real-time by an optimized C algorithm embedded in LabVIEW, which can handle RD event rates on the order of 10 kHz on a standard computer.

As shown in the lower panel of Fig. 3, the fit residuals from a single RD event exhibit an exponentially decaying shot noise component at the beginning of the ring-down. It is due to the Poissonian nature of the coherent laser field and dominates for the first few RD times after the trigger, indicating a near-shot-noise-limited measurement. Further evidence for this and a more detailed discussion of the shot-noise-limit are given in Sect. 3.1. Averaging over many fit residuals cancels the random shot-noise and ADC noise components and reveals a static pattern. This structure is stable in time and attributed to ADC nonlinearity well within the acquisition card specifications. The associated relative systematic error [37] amounts to 5×10^{-6} in the present case.

2.3 Automated spectrometer operation

In order to allow acquisition of broadband spectra and long-term averaging, the spectrometer operation has been

Fig. 3 *Upper panel* Ring-down cavity transmission under Pound-Drever-Hall-locking conditions with ring-down triggering by the *black* signal (*orange background*). *Lower panel* Residuals from exponential least-squares fit of a ring-down signal. Averaging of 10^4 (*black*) and 10^5 (*white*) successive fit residuals reveals a static pattern attributed to acquisition card nonlinearity
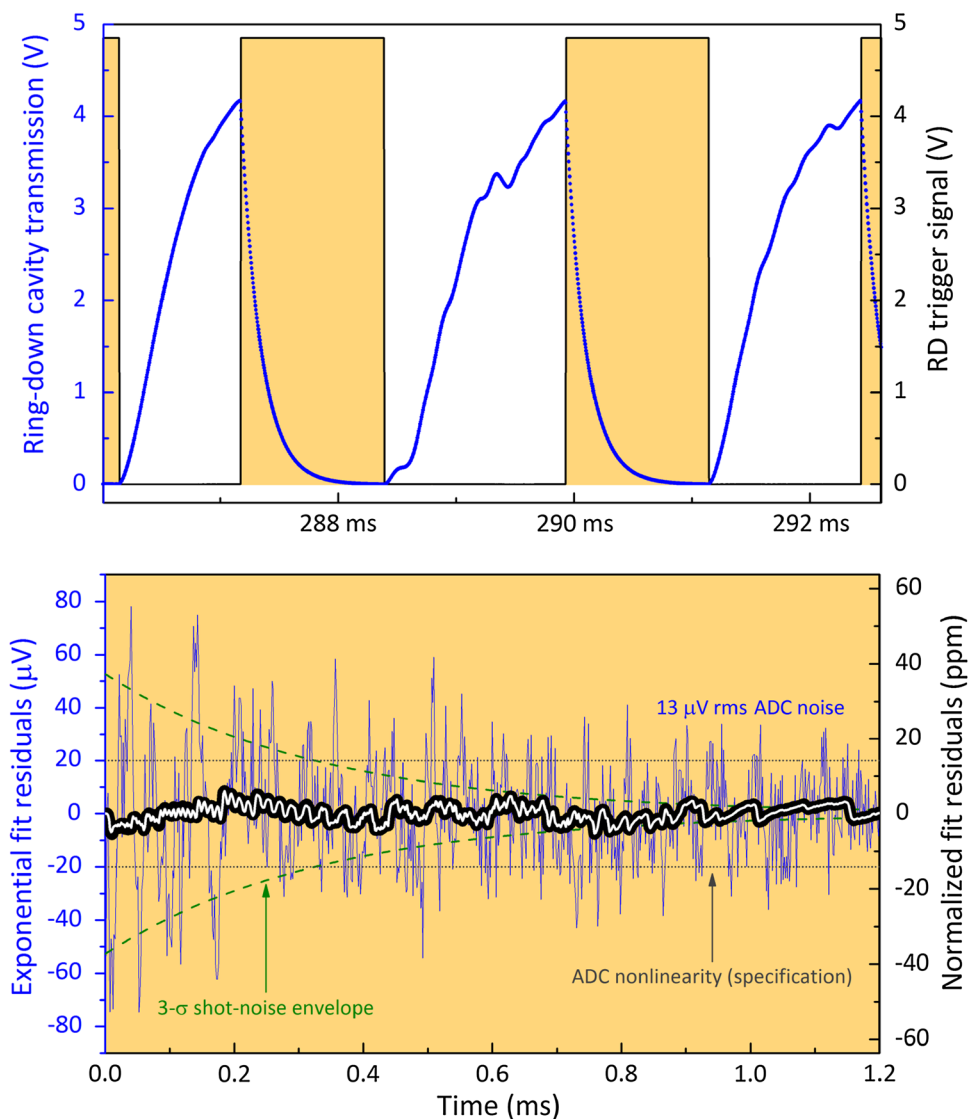
completely automated using a dedicated LabVIEW software. Its basic principle is to acquire an absorption spectrum by measuring many RD events at one laser frequency and subsequently stepping to the next frequency, while logging experimental parameters such as time, pressure and temperature. Looping this procedure yields time-resolved or averaged spectral information. An overview of the automatization tasks is given in the following.

The laser frequency is changed by means of an optimized combination of the elements of Eq. (2). Rapid fine-tuning by single-sideband modulation at the computer-controlled synthesizer frequency ν_{RF} is complemented by FSR-by-FSR tuning as soon as the RF tuning range is left. To change the V-cavity mode k, a laser current sweep controlled by a digital-to-analog converted (DAC) voltage is applied to the DC modulation input of the current driver. When the limit of current-based laser frequency tuning is reached after roughly 15 GHz, the system automatically

stabilizes to a new laser diode temperature to connect the next current-scanning interval. This tuning scheme enables an arbitrary frequency stepping resolution limited only by laser drift and linewidth. One may choose uniform frequency steps for survey-type broadband spectra (cf. Sect. 3.2) or an adaptive measurement frequency grid in the case of known spectra, in particular for isolated lines (cf. Sect. 3.3). This allows choosing a distribution of points which optimizes the measurement precision for a given parameter, such as width or integrated absorption, and a given measurement time. For carrying out the latter type of measurement, the spectrometer first acquires a rapid survey spectrum at uniform frequency steps. The software then determines an adaptive measurement frequency grid which is subsequently used for repeatedly acquiring spectra of that spectral interval.

After tuning the laser frequency, Pound-Drever-Hall lock of the cavity is acquired by means of a DAC-controlled

PZT-voltage sweep which localizes the TEM_{00} mode of the ring-down cavity. The corresponding high-voltage offset is then kept constant, while the analog servo loop takes over and locks the system. Once lock is acquired within roughly half a second, ring-downs are triggered, acquired and fitted in real time at kHz-level rates. In order to average out the RD time bias due to an interference fringe from the return losses of the fiber-optic circulator, the distance between circulator and cavity is triangle-modulated by means of a PZT-mounted steering mirror. The impact of this active fringe cancelation scheme will be discussed in detail in Sect. 3.1. For known spectral regions, the length of the laser-off RD acquisition period is automatically adapted to be a fixed multiple of the RD time τ. At the RD signal-to-noise ratio (SNR) of Fig. 3, for instance, ten RD times are sufficient for optimal exponential fit precision. The quality of RD residuals is checked for ensuring that there is no resonant injection of the residual carrier or other sideband into cavity transverse modes, whose geometric overlap with the laser beam [38] is at the permil level. In practice, this situation virtually never arises due to the high-cavity finesse and the strong suppression of unwanted spectral components at the MZM output. For frequency steps exactly equal to one RD cavity FSR or smaller than the PDH locking range of $\pm\nu_{PDH}$, as in the case of saturated-absorption spectra [23], the system remains locked after changing the RF. As no relock procedure is required in these cases, they are chosen whenever very small or rather big (cf. baseline of Fig. 7) frequency steps are applicable.

In order to ensure well-defined experimental conditions, the ring-down cavity is actively temperature stabilized, currently by means of a stand-alone ventilated Peltier cooler (Laird AA-040-1222) regulating the reading from a $100\,\Omega$ platinum temperature probe (PT100) contacted to the cavity surface. For the follow-up setup under development, six $1\,k\Omega$ platinum probes (PT1000) will be deployed in a uniform distribution centimeter deep within the cavity bulk for low-noise temperature stabilization and residual temperature gradient monitoring.

The pressure inside the RD cavity is monitored using a 10 Torr Baratron gauge (MKS 626B). A completely automated pumping and gas inlet system based on solenoid and pneumatic valves is under development. Enabling completely automated spectrometer operation and remote control, this will notably allow for regular nitrogen flushing and cycling of calibration gas and sample gas for optical isotopic ratio measurements.

3 Results

The OFFS-CRDS prototype was used for a series of proof-of-principle experiments, which will be discussed in the following, characterizing its performance and illustrating its potential for absorption line metrology applications.

3.1 Absorption measurement precision, stability and fringe scrambling

The measurement stability can be characterized by means of a two-sample variance approach originally developed for estimating the stability of frequency standards by Allan [39]. The concept has been applied to absorption measurements by Werle et al. [40] to quantify the limitations of noise reduction by averaging in the presence of instrumental drifts. The Allan-Werle deviation for ring-down measurements by OFFS-CRDS, expressed in absorption coefficient units, as a function of averaging time is depicted in Fig. 4.

Fig. 4 Allan-Werle deviation characterizing the ring-down absorption measurement stability. The *x* axis corresponding to the number of averaged measurements *N* has been expressed in units of time here to facilitate comparison. The *inset* shows the time series of ring-down events corresponding to the respective experimental Allan-Werle deviations
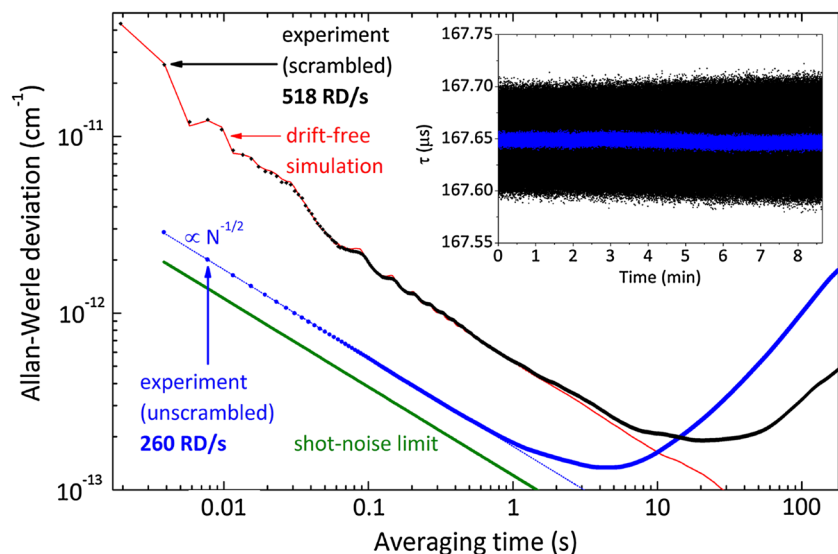
The blue circles, corresponding to the time series shown in the inset, is the Allan-Werle deviation recorded without moving the circulator-cavity fringe-scrambling PZT. Starting at a single-shot precision of 3×10^{-12} cm^{-1}, it reaches its minimum at 1.4×10^{-13} cm^{-1} after 4 s. Beyond this point, the drift due to the circulator-cavity fringe becomes dominant. For shorter averaging times, the Allan-Werle deviation is inversely proportional to the square root of the number of averages N and remarkably close to the photo-electron shot noise (green line).

To derive this fundamental limit for CRDS [41], let us consider the photocurrent $I(t)$ during a RD event

$$I(t) = \frac{V_0}{R} e^{-t/\tau} \tag{3}$$

yielding a voltage $V(t) = RI(t)$ at the transmission PD transimpedance amplifier gain resistance R. Sampling $V(t)$ by an ADC at time intervals t_s with a gate time t_g yields a discrete time series V_k related to the number Q_k of photoelectrons accumulated during the gate time. Expressing Q_k in terms of the photocurrent and the elementary charge e yields

$$Q_k = \frac{1}{e} \int_{kt_s}^{kt_s+t_g} I(t)\mathrm{d}t \approx \frac{V_0 t_g}{eR} e^{-kt_s/\tau} \tag{4}$$

The last equality holds in good approximation for $t_g \ll \tau$. Q_k exhibits random fluctuations due to the quantum character of the coherent light field and the random nature of photo-electron generation. The standard deviation σ_{Q_k} of this Poissonian photo-electron shot noise process is

$$\sigma_{Q_k} = \sqrt{Q_k} \tag{5}$$

Determining the RD time τ by means of an exponential fit of the infinite digitized voltage time series V_k can be formulated as a linear regression on the natural logarithm of the dimensionless charge Q_k according to Eq. (4):

$$y_k \equiv \ln Q_k = \ln\left(\frac{V_0 t_g}{eR}\right) - \frac{t_s}{\tau}k \equiv A + Bk \tag{6}$$

Obtaining a maximum-likelihood estimate for τ implies minimizing the sum $\sum_{k=0}^{\infty}\left((y_k - \overline{y_k})/\sigma_{y_k}\right)^2$ of normalized differences between data y_k and model $\overline{y_k}$, with $\sigma_{y_k} = 1/\sqrt{Q_k}$ by simple error propagation of Eq. (5) in Eq. (6). This weighted least-squares fit has an analytic solution [42] which allows error propagation on the fit parameters A and B by using the geometric series and related expressions. Converting σ_B to σ_τ and expressing in absorption units σ_α through Eq. (1) yields the CRDS shot-noise limit

$$\sigma_\alpha = \sqrt{\frac{eR}{V_0 c^2 \tau^3} \frac{t_s}{t_g}} = \alpha\sqrt{\frac{eRt_s}{V_0 \tau t_g}} \tag{7}$$

In the present case, $t_s^{-1} = 650$ kHz, $t_g = 1$ μs, $V_0 = 1.4$ V, $R = 90,900\ \Omega$ and $\tau = 167$ μs lead to a shot-noise limit of 2×10^{-12} cm^{-1} for single-RD precision. An important practical consequence of this analysis is that a weighted exponential fit has to be employed in the near-shot-noise-limited regime to reach optimal precision. In practice, Allan-Werle deviations of RD time series from unweighted exponential fitting were up to 50 % higher than those based on a true maximum-likelihood estimate for the present setup.

The black diamonds in Fig. 4 are the Allan-Werle deviation derived from RD events under fringe-scrambling conditions, reaching a minimum of 1.9×10^{-13} cm^{-1} after 20 s. Exploring all possible values of the circulator interference fringe by varying its phase through the scrambling PZT position significantly increases RD time fluctuations, as clearly visible on the time series in the inset. This pseudo-noise is counterbalanced by a shorter RD acquisition period which increases the RD repetition rate, thereby leading to efficient averaging with a characteristic oscillatory behavior.

The shape of this Allan-Werle deviation can be modeled in terms of a Monte-Carlo simulation of fringe-scrambled RD measurements α_k based on the ansatz

$$\alpha_k = \alpha_0 + \Delta_\alpha \sin\left(2\pi d \times \mathrm{tri}(t_k, f_s) + \varphi_s\right) + \epsilon_k \tag{8}$$

$$t_k = t_{k-1} + f_{\mathrm{RD}}^{-1} + \xi_k \tag{9}$$

where $\mathrm{tri}(t, f_s)$ is a symmetric triangle function with amplitude ± 1 and periodicity f_s^{-1} evaluated at time t. ε_k and ξ_k are random numbers with zero mean representing RD measurement noise and non-uniform RD timing, respectively. The scrambling frequency $f_s = 17$ Hz and the RD event rate $f_{\mathrm{RD}} = 518$ Hz are imposed by the measurement conditions of Fig. 4. The fringe amplitude $\Delta_\alpha = 5 \times 10^{-11}$ cm^{-1}, the PZT-scrambling modulation depth $d \approx 2.5$ controlled by the high voltage applied to the PZT, as well as the 8.5×10^{-12} cm^{-1} standard deviation of ε_k were equally fixed to experimental values. The fringe offset $\varphi_s = 1.25$, $t_0 = 0$, and the range $|\xi_k| \leq 625$ μs of possible RD timing jitter values were manually adjusted to the data. The excellent agreement between the experimental Allan-Werle deviation and the one calculated from the simulated absorption coefficient time series α_k indicates that the averaging behavior under fringe-scrambling conditions is well understood in terms of the physical processes formalized by Eqs. (8) and (9).

An Allan-Werle plot such as the one in Fig. 4, based on measurements at one single frequency, can be misleading in the presence of optical fringes. Taken in itself, it is thus insufficient for characterizing frequency-scanned spectrometer performance. In this regime, a systematic analysis of spectrometer baseline structure is vital to
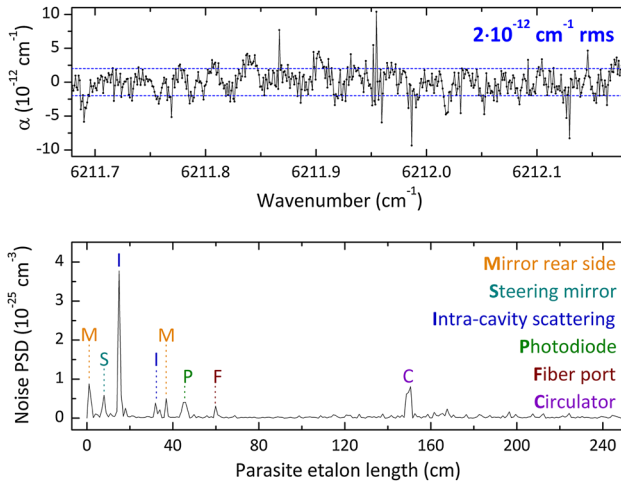
Fig. 5 Spectrometer baseline after linear correction (*upper panel*). The corresponding absorption noise power spectral density (*lower panel*) reveals interference by parasite reflections with different etalon lengths

analyze and minimize the impact of interference fringes due to parasite reflections. For the present OFFS-CRD spectrometer, the 0.5 cm^{-1} wide baseline section shown in the upper panel of Fig. 5 was recorded at frequency steps of 10^{-3} cm^{-1}. Measuring for 1.5 s at each point yielded 300 RD events on average, resulting in a baseline rms noise level of only 2×10^{-12} cm^{-1}. The improvement in comparison with the first demonstration [23] is due to a meticulous optimization of alignment and cleaning of all optics, the use of a quarter-wave plate between cavity and photodiode, as well as a more sophisticated fringe cancelation procedure.

This scheme exploits the fact that the RD time bias due to the interference fringe changes sign when the phase of the latter changes by $\pm\pi$. In analogy to Eq. (8), the bias Δ_α of the absorption measurement due to two fringes Δ_{α_a} and Δ_{α_b} may be generalized as

$$\Delta\alpha = \Delta_{\alpha_a} \sin\left(\frac{4\pi p}{\lambda} + \phi_a\right) + \Delta_{\alpha_b} \sin\left(\frac{8\pi p}{\lambda} + \phi_b\right) \quad (10)$$

by expressing the parameter d in terms of the scrambling PZT displacement p. In the paraxial approximation, d is roughly equal to $2p/(\lambda/2)$ for an interference fringe having its origin before the last steering mirror, represented by Δ_{α_b}, and $p/(\lambda/2)$ for parasite scattering by the steering mirror itself, represented by Δ_{α_a}.

In order to cancel the effect of both fringes, the PZT may therefore be stepped to four positions $p_j = j \times \lambda/8$ with $j = 0, \ldots, 3$, yielding fringe contributions with opposite signs. The arithmetic mean $\overline{\Delta_\alpha}$ of the corresponding Δ_{α_j} is thus zero, corresponding to complete fringe canceling:

$$\overline{\Delta_\alpha} = \frac{1}{4} \sum_{j=0}^{3} \Delta_{\alpha_j} = \frac{\Delta_{\alpha_a}}{4} \sum_{j=0}^{3} \cos\left(\phi_a + j\frac{\pi}{2}\right)$$

$$+ \frac{\Delta_{\alpha_b}}{4} \sum_{j=0}^{3} \cos\left(\phi_b + j\pi\right) = 0 \quad (11)$$

In practice, $\overline{\Delta_\alpha}$ is determined by averaging N_j RD measurements at each position p_j.

$$\Delta_{\alpha_j} = \frac{1}{N_j} \sum_{i=1}^{N_j} \Delta_{\alpha_{j_i}} \quad (12)$$

The random noise σ_α on the $\Delta_{\alpha_{j_i}}$ values propagates to $\overline{\Delta_\alpha}$ as

$$\sigma_{\overline{\Delta_\alpha}} = \frac{\sigma_\alpha}{4} \sqrt{\sum_{j=0}^{3} \frac{1}{N_j}} \quad (13)$$

via Eqs. (11) and (12). In the optimal case $N_j = N/4 \; \forall j$, this fringe cancelation method therefore yields a RD measurement precision equal to the one for N fringe-biased measurements at a single displacement p. In practice, care has to be taken to keep the number of RD events close to $N/4$ for all spectral measurement points, since noise increases considerably for a non-uniform N_j distribution according to Eq. (13). Small deviations from N_j-uniformity are irrelevant in a regime where RD acquisition noise is negligible compared with optical fringes. This is clearly the case for the present near-shot-noise-limited spectrometer with kHz-level repetition rates.

For the sake of generality, let us nonetheless note that the present scheme can be beneficially applied also in a regime where random acquisition noise dominates over interference fringes, even if the N_j are non-uniform. In this special case, the weighting in Eq. (11) should be modified to read

$$\overline{\Delta_\alpha} = \frac{\sum_{j=0}^{3} N_j \Delta_{\alpha_j}}{\sum_{j=0}^{3} N_j} \quad (14)$$

While this compensation strategy leads to only partial fringe cancelation, it has the benefit of not impairing the statistical noise reduction due to averaging.

As shown in the lower panel of Fig. 5, converting the baseline noise to a power spectral density (PSD) by Fourier transform clearly reveals several periodic contributions. With the help of the etalon length corresponding to these peaks in the PSD, the optics responsible for each parasite reflection may be identified. In the present case, small signatures of the FC-APC fiber out-coupling, the anti-reflection-coated, wedged rear side of the dielectric cavity mirrors, as well as the transmission photodiode can be discerned. A small residual from the scrambled circulator fringe is also still visible. The dominant 15 cm-fringe

is presumedly due to intra-cavity scattering losses. This hypothesis will be checked by means of the slightly different RD cavity design of a follow-up setup.

3.2 Broadband spectrum of CO_2 at 1.6 µm

OFFS-CRDS was used for acquiring the broadband, high-resolution spectrum of carbon dioxide around 1.6 µm shown in Fig. 6. This 17 h measurement was carried out for CO_2 at natural isotopic abundances and a partial pressure of 10 Pa for optimally exploiting the dynamic range of the spectrometer. Being defined as the ratio of the biggest signal to the noise on the baseline, this quantity amounts to almost 8×10^5 in the present case, with a baseline noise as low as 4×10^{-12} cm^{-1}. The inverted red curve in Fig. 6a shows a simulated spectrum based on the HITRAN 2012 database [43] for comparison.

For lines in the $40013 \leftarrow 10001$ hot band of $^{12}C^{16}O_2$, the measured spectrum reveals significant disagreements with the center frequencies from the HITRAN database. For instance, the center of the R6 line shown in Fig. 6b was determined to be 6,210.7097(5) cm^{-1} and clearly disagrees with the HITRAN value of 6,210.7126 cm^{-1} given at an accuracy better than 10^{-3} cm^{-1}. Our value is in excellent agreement with previous CRDS measurements [5] (6,210.7094(10) cm^{-1}) and the position calculated from the band parameters by Miller and Brown [44] (6,210.7096(4) cm^{-1}), consequently underpinning the need for a revision of HITRAN values for this band.

A more comprehensive evaluation of the spectrum in Fig. 6 is in progress. It is expected to yield sub-MHz line center accuracies also for weak bands by using absolute frequency references at 1.6 µm.
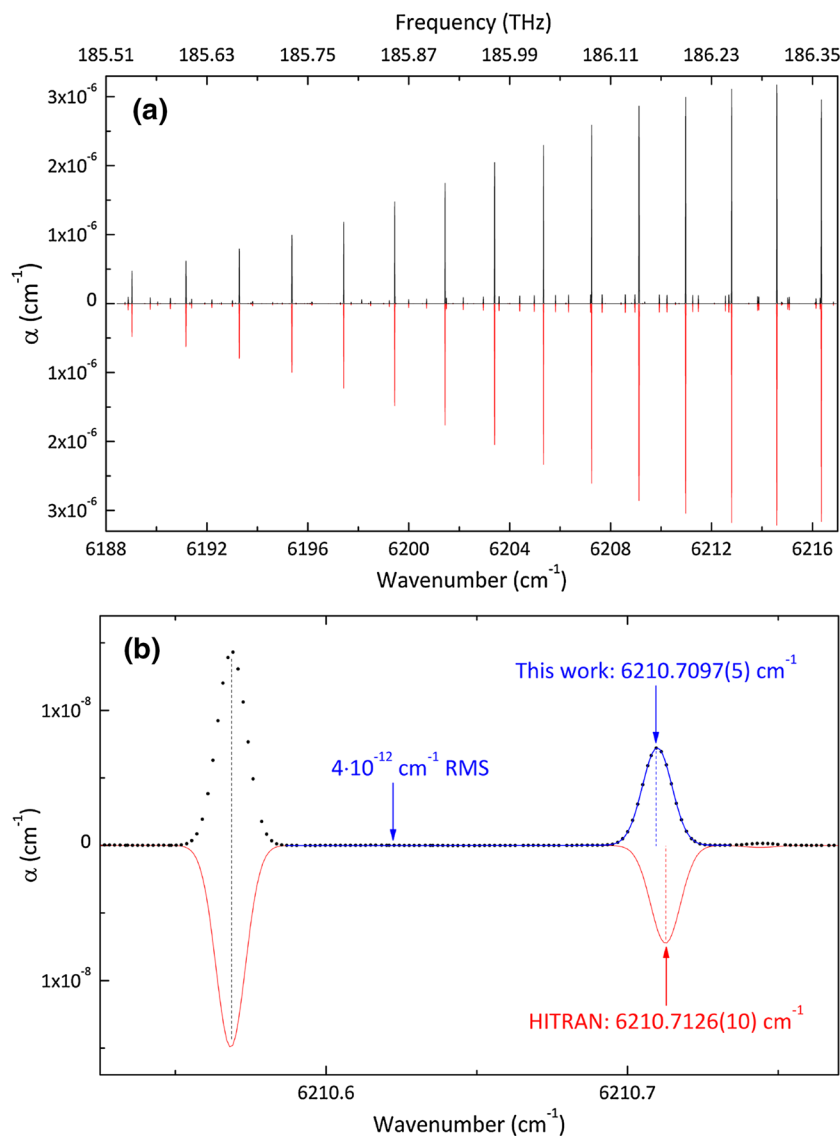

Fig. 6 a *Black curve* Measured broadband absorption spectrum in the P-branch of the $30013 \leftarrow 00001$ band of CO_2 at 10 Pa and 296 K with second-order polynomial baseline correction. The frequency stepping resolution was 50 MHz, with several hundreds of RD events averaged for each point. *Red curve* Simulated HITRAN spectrum at identical conditions. **b** Zoom showing the individual data points and the spectrum baseline noise. The $40013 \leftarrow 10001$ R6 line at 6210.71 cm^{-1} exhibits a significant frequency offset with respect to the HITRAN value

Fig. 7 Isolated $30013 \leftarrow 00001$ P16 line of CO_2 at $6{,}214.588$ cm^{-1} broadened by N_2 at a total pressure of 150 Pa and a CO_2 concentration of 5.04×10^{-3}, with first-order polynomial baseline correction. The *lower panels* show the fit residuals from different line profile models. Fit quality is indicated as the ratio QF of peak signal to rms fit residuals
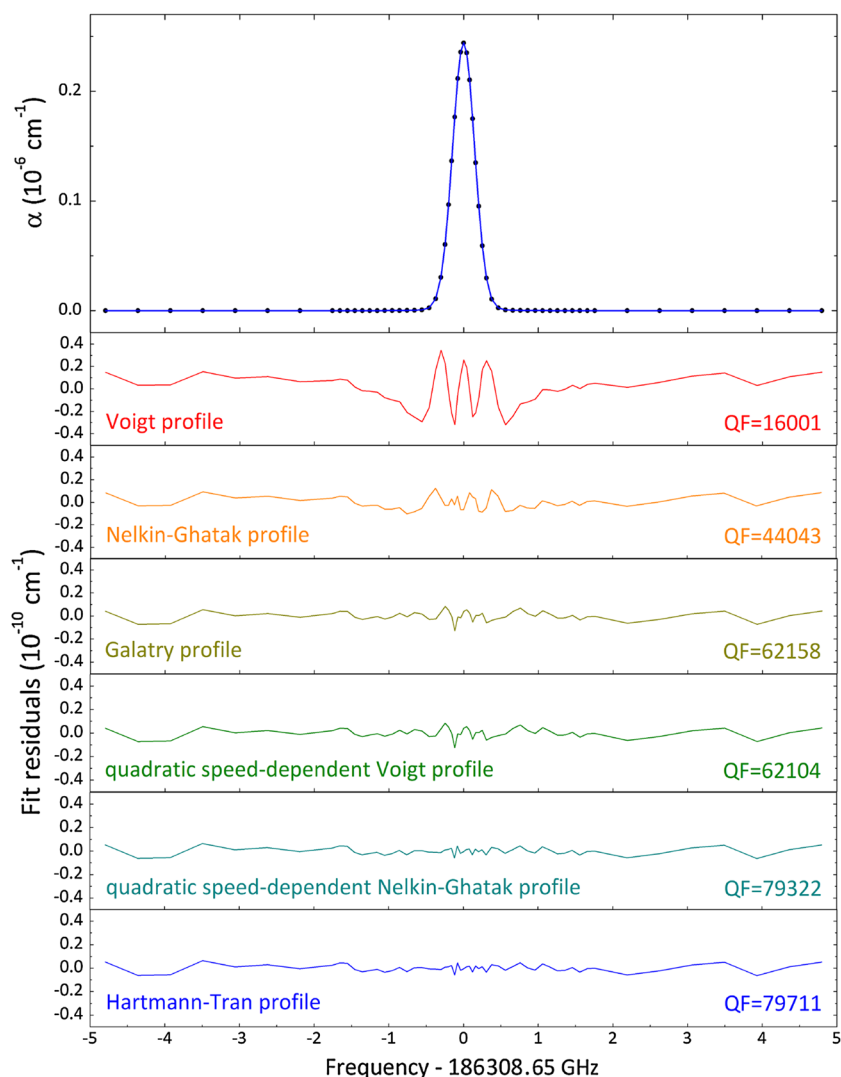
3.3 Isolated line-shape study of CO_2 in N_2

A precision lineshape measurement of CO_2 broadened by N_2 was carried out at a temperature of 295.8 ± 0.1 K and a pressure of 150 Pa, with a CO_2 mole fraction of 5.04×10^{-3}. The 3.6 min single scan depicted in Fig. 7 was recorded with adaptive measurement parameters, such as the number of averaged RD events and the frequency stepping between 40 and 434.4 MHz. It exhibits a SNR of almost 8×10^4. The experimental data were fitted with various common line-shape models to compare their performance. In view of the high SNR, all parameter were kept floating during fitting. With the molecular mass m and the Boltzmann constant k_B, the fitted Doppler width Δ_D allows a critical comparison of the corresponding Doppler temperature $T_D = (\Delta_D/\nu)^2 mc^2/k_B$ to the measured RD cavity temperature. The fit residuals are shown in the lower panels of Fig. 7 and the deduced physical parameters are reported in Table 1. As a semi-quantitative indicator for fit quality,

Table 1 Comparison of the models used for fitting the line profile in Fig. 7.

Profile	QF	T_D (K)	$10^4 \Gamma$ (cm^{-1})	$10^9 A$ (cm^{-2})
Voigt	16001	293.37	1.335	3.0590
NG	44043	294.56	1.353	3.0575
Galatry	62158	296.40	1.249	3.0564
qSD Voigt	62104	296.41	1.248	3.0564
qSDNG	79322	295.90	1.275	3.0567
pCqSDNG	79711	295.91	1.338	3.0567

QF fit quality figure, T_D Doppler temperature, Γ Lorentzian width, *A* integrated absorption, *NG* Nelkin-Ghatak, *qSD* quadratic speed-dependent, *pC* partially correlated

the quality figure (QF) defined as the ratio between peak signal and rms fit residuals [21] was adopted. Depending on the distribution of spectral points, QF may constitute a somewhat ambiguous measure. Nevertheless, it is a

sensitive and meaningful fit quality indicator for the present study, as most measurement points were taken close to the line center.

The characteristic residuals from fitting with a Voigt profile clearly show its inadequacy even at this rather low pressure, underlined by the severely biased Doppler temperature (2.4 ± 0.1 K) below the true value.

As a first refinement beyond the Voigt profile, velocity-changing collisions leading to collisional (Dicke) narrowing [45] are often taken into account by means of the hard-collision Nelkin-Ghatak model [46]. In the present case, its fit residuals are significantly flatter than for the Voigt profile, but retain a considerable systematic structure. This is reflected by the biased Doppler temperature deduced from the fit, which is still wrong by 1.2 ± 0.1 K. The Galatry profile [47] is based on a complementary approach to collisional narrowing considering soft collision leading to only slight velocity changes. Here, it yields further improved fit residuals, which feature only little residual structure. Nonetheless, this seemingly good agreement is accompanied by a significantly biased Doppler temperature retrieval off by 0.6 K. These observations indicate that collisional narrowing alone is not sufficient to describe the physics underlying the observed lineshape.

Line-narrowing can also be due to the speed-dependence of the collisional width and shift. This is taken into account in a quadratic approximation by fitting with the quadratic speed-dependent Voigt profile. Although based on an entirely different physical mechanism, the residuals and parameters from this fit are very similar to those obtained with the Galatry profile. Combining both collisional narrowing and speed-dependence by the quadratic speed-dependent Nelkin-Ghatak (qSDNG) profile leads to a further, significant improvement in fit quality. Importantly, the Doppler temperature derived from this fit is consistent with the resistive temperature probe measurement. The residuals are flat over the whole scanning range, yielding the true SNR of the measurement, and indicating that the introduction of further parameters should create parameter correlations without improving the fit quality. This is the case when fitting with the so-called Hartmann-Tran profile (HTP) [48], which generalizes the qSDNG profile by including a partical correlation between velocity-changing and dephasing collisions (pCqSDNG). It has been suggested that this profile should supersede the Voigt profile in databases for atmospheric applications and radiative transfer models [49], as it preserves backward compatility and features a very limited computational cost, with seven parameters which are either independent of or proportional to pressure. The HTP yields results in terms of fit quality and Doppler temperature which are very similar to those obtained with the qSDNG, but their Lorentzian broadenings Γ differ by almost 5 %. To resolve this ambiguity, a multi-fit procedure combining spectra at different pressures should be carried out, ideally from the Doppler-limited to near-Lorentzian regimes. By taking the physical scaling of parameters with pressure into account, this approach allows resolving the correlations between single-spectrum fit parameters [48] and is to be recommended for reliably retrieving physically meaningful quantities. Nevertheless, we have demonstrated here that a spectrometer with a very high signal-to-noise ratio distinguishes between the different physical broadening and narrowing processes in a remarkably efficient manner already on a single-line basis. The differences between the retrieved integrated absorption areas, which are at the 10^{-4} level even for profiles beyond Voigt, suggest the cautious use of advanced profiles for applications such as trace gas monitoring and isotopic ratio measurements.

4 Conclusions

OFFS-CRDS combines an adaptive resolution down to the kHz-level with a near-shot-noise-limited absorption sensitivity of 2×10^{-13} cm^{-1}/$\sqrt{\text{Hz}}$, and allows recording broadband spectra over a 1 THz span with an rms baseline noise as low as 2×10^{-12} cm^{-1}. This performance makes it a versatile, powerful tool for absorption line metrology. For achieving optimal performance, a thorough minimization of interference fringes due to parasite reflections is crucial. To this end, two active fringe cancelation schemes based on triangle-shaped and discrete piezoelectric mirror displacements were experimentally realized and theoretically described.

The OFFS-CRDS prototype was used for recording a high-resolution spectrum of CO_2, with a dynamic range approaching 800,000, between 6,188 and 6,217 cm^{-1}, confirming a need for improvement of the line center frequencies of the $^{16}O^{12}C^{16}O$ 40013 $\leftarrow$ 10001 hot band in the HITRAN 2012 database. By linking OFFS-CRDS to absolute frequency references of any type, such high-resolution survey-type spectra should allow broadband line center frequency measurements with sub-MHz accuracy even for weak bands.

We measured the spectrum of an isolated transition of CO_2 broadened by N_2 with adaptive resolution and a signal-to-noise ratio of 80,000, clearly distinguishing line-narrowing effects beyond the Voigt profile at a pressure of 150 Pa. This performance opens the door to a systematic multi-fit analysis of line measurements over whole absorption bands and wide pressure ranges, for validating state-of-the-art lineshape models and retrieving accurate, physically meaningful line parameters. To harness this potential for applications in environmental sciences, we are currently developing an OFFS-CRD spectrometer dedicated to carbon dioxide isotopic ratios measurements.

Due to its tightly locked high-finesse ring-down cavity, OFFS-CRDS features kW/cm²-level intracavity light intensity for input powers on the order of 100 μW. We demonstrated elsewhere [23] how this can be exploited for saturating weak CO_2 transitions around 1.6 μm involving four vibrational quanta. In a setup linked to a self-referenced frequency comb, such sub-Doppler Lamb dip measurements could pave the way to extensive near-infrared line center retrievals with sub-kHz-accuracy. This is expected to yield a multitude of new frequency references for precision spectroscopy and to contribute to the verification of state-of-the-art *ab-initio* energy level calculations.

Beside these promising lab-based applications, the relatively compact and rugged experimental setup, which uses fiber-optic components to a great extent, calls for mobile, field-deployable spectrometers. The development of such an OFFS-CRDS instrument for monitoring the concentration and isotopic composition of water vapor in Antarctic air is currently underway.

References

1. D. Romanini, A. Kachanov, N. Sadeghi, F. Stoeckel, Chem. Phys. Lett. **264**, 316 (1997)
2. S. Kassi, A. Campargue, J. Chem. Phys. **137**, 234201 (2012)
3. L. Brown, K. Sung, D. Benner, V. Devi, V. Boudon, T. Gabard, C. Wenger, A. Campargue, O. Leshchishina, S. Kassi, D. Mondelain, L. Wang, L. Daumont, L. Rgalia, M. Rey, X. Thomas, V.G. Tyuterev, O. Lyulin, A. Nikitin, H. Niederer, S. Albert, S. Bauerecker, M. Quack, J. OBrien, I. Gordon, L. Rothman, H. Sasada, A. Coustenis, M. Smith, T. C Jr, X.-G. Wang, A. Mantz, P. Spickler, J. Quant. Spectrosc. Radiat. Transf. **130**, 201 (2013)
4. S. Mikhailenko, D. Mondelain, S. Kassi, A. Campargue, J. Quant. Spectrosc. Radiat. Transf. **140**, 48 (2014)
5. B. Perevalov, S. Kassi, V. Perevalov, S. Tashkun, A. Campargue, J. Mol. Spectrosc. **252**, 143 (2008)
6. E. Crosson, Appl. Phys. B **92**, 403 (2008)
7. E. Kerstel, L. Gianfrani, Appl. Phys. B **92**, 439 (2008)
8. E.T. Kerstel, R. Iannone, M. Chenevier, S. Kassi, H.-J. Jost, D. Romanini, Appl. Phys. B **85**, 397 (2006)
9. J. Landsberg, D. Romanini, E. Kerstel, Opt. Lett. **39**, 1795 (2014)
10. D. Long, M. Okumura, C. Miller, J. Hodges, Appl. Phys. B **105**, 471 (2011)
11. Y. Chen, K.K. Lehmann, J. Kessler, B.S. Lollar, G.L. Couloume, T.C. Onstott, Anal. Chem. **85**, 11250 (2013)
12. A.L. Rizzo, H.-J. Jost, A. Caracausi, A. Paonita, M. Liotta, M. Martelli, Geophys. Res. Lett. **41**, 2382 (2014)
13. O.L. Polyansky, A.G. Császár, S.V. Shirin, N.F. Zobov, P. Barletta, J. Tennyson, D.W. Schwenke, P.J. Knowles, Science **299**, 539 (2003)
14. A. Campargue, S. Kassi, K. Pachucki, J. Komasa, Phys. Chem. Chem. Phys. **14**, 802 (2012)
15. A. Pogány, O. Ott, O. Werhahn, V. Ebert, J. Quant. Spectrosc. Radiat. Transf. **130**, 147 (2013)
16. J.T. Hodges, R. Ciuryło, Rev. Sci. Instrum. **76**, 023112 (2005)
17. D. Long, A. Cygan, R. van Zee, M. Okumura, C. Miller, D. Lisak, J. Hodges, Chem. Phys. Lett. **536**, 1 (2012)
18. D. Lisak, J.T. Hodges, Appl. Phys. B **88**, 317 (2007)
19. M.D. De Vizia, A. Castrillo, E. Fasci, P. Amodio, L. Moretti, L. Gianfrani, Phys. Rev. A **90**, 022503 (2014)
20. J.-M. Hartmann, H. Tran, N.H. Ngo, X. Landsheere, P. Chelin, Y. Lu, A.-W. Liu, S.-M. Hu, L. Gianfrani, G. Casa, A. Castrillo, M. Lepère, Q. Delière, M. Dhyne, L. Fissiaux, Phys. Rev. A **87**, 013403 (2013)
21. P. Wcisło, A. Cygan, D. Lisak, R. Ciuryło, Phys. Rev. A **88**, 012517 (2013)
22. P. Wcisło, H. Tran, S. Kassi, A. Campargue, F. Thibault, R. Ciuryło, J. Chem. Phys. **141**, 074301 (2014)
23. J. Burkart, D. Romanini, S. Kassi, Opt. Lett. **39**, 4695 (2014)
24. C.J. Bordé, Phil. Trans. R. Soc. A **363**, 2177 (2005)
25. C. Daussy, M. Guinet, A. Amy-Klein, K. Djerroud, Y. Hermier, S. Briaudeau, C. Bordé, C. Chardonnet, Phys. Rev. Lett. **98**, 250801 (2007)
26. L. Moretti, A. Castrillo, E. Fasci, M.D. De Vizia, G. Casa, G. Galzerano, A. Merlone, P. Laporta, L. Gianfrani, Phys. Rev. Lett. **111**, 060803 (2013)
27. S. Kassi, M. Chenevier, L. Gianfrani, A. Salhi, Y. Rouillard, A. Ouvrard, D. Romanini, Opt. Express **14**, 11442 (2006)
28. W.E. Wang, A.P.M. Michel, L. Wang, T. Tsai, M.L. Baeck, J.A. Smith, G. Wysocki, Rev. Sci. Instrum. **85**, 093103 (2014)
29. B. Tuzson, J. Mohn, M. Zeeman, R. Werner, W. Eugster, M. Zahniser, D. Nelson, J. McManus, L. Emmenegger, Appl. Phys. B **92**, 451 (2008)
30. J. Burkart, D. Romanini, S. Kassi, Opt. Lett. **38**, 2062 (2013)
31. B. Dahmani, L. Hollberg, R. Drullinger, Opt. Lett. **12**, 876 (1987)
32. P. Laurent, A. Clairon, C. Breant, IEEE J. Quant. Electron. **25**, 1131 (1989)
33. M. Izutsu, S. Shikama, T. Sueta, IEEE J. Quant. Electron. **17**, 2225 (1981)
34. T. Udem, R. Holzwarth, T.W. Hänsch, Nature **416**, 233 (2002)
35. D.Z. Anderson, J.C. Frisch, C.S. Masser, Appl. Opt. **23**, 1238 (1984)
36. R.W.P. Drever, J.L. Hall, F.V. Kowalski, J. Hough, G.M. Ford, A.J. Munley, H. Ward, Appl. Phys. B **31**, 97 (1983)
37. S. Wójtewicz, D. Lisak, A. Cygan, J. Domysławska, R. Trawiński, R. Ciuryło, Phys. Rev. A **84**, 032511 (2011)
38. D. Romanini, Appl. Phys. B **115**, 517 (2014)
39. D.W. Allan, Proc. IEEE **54**, 221 (1966)
40. P. Werle, R. Mücke, F. Slemr, Appl. Phys. B **57**, 131 (1993)
41. D. Romanini, K. Lehmann, J. Chem. Phys. **99**, 6287 (1993)
42. J. Taylor, *Introduction to Error Analysis, the Study of Uncertainties in Physical Measurements* (University Science Books, New York, 1997)
43. L. Rothman, I. Gordon, Y. Babikov, A. Barbe, D.C. Benner, P. Bernath, M. Birk, L. Bizzocchi, V. Boudon, L. Brown, A. Campargue, K. Chance, E. Cohen, L. Coudert, V. Devi, B. Drouin, A. Fayt, J.-M. Flaud, R. Gamache, J. Harrison, J.-M. Hartmann, C. Hill, J. Hodges, D. Jacquemart, A. Jolly, J. Lamouroux, R.L. Roy, G. Li, D. Long, O. Lyulin, C. Mackie, S. Massie, S. Mikhailenko, H. Mller, O. Naumenko, A. Nikitin, J. Orphal, V. Perevalov, A. Perrin, E. Polovtseva, C. Richard, M. Smith, E. Starikova, K. Sung, S. Tashkun, J. Tennyson, G. Toon, V. Tyuterev, G. Wagner, J. Quant. Spectrosc. Radiat. Transf. **130**, 4 (2013)
44. C.E. Miller, L.R. Brown, J. Mol. Spectrosc. **228**, 329 (2004)
45. R.H. Dicke, Phys. Rev. **89**, 472 (1953)
46. M. Nelkin, A. Ghatak, Phys. Rev. **135**, A4 (1964)

47. L. Galatry, Phys. Rev. **122**, 1218 (1961)
48. N. Ngo, D. Lisak, H. Tran, J.-M. Hartmann, J. Quant. Spectrosc. Radiat. Transf. **129**, 89 (2013)
49. J. Tennyson, P.F. Bernath, A. Campargue, A.G. Császár, L. Daumont, R.R. Gamache, J.T. Hodges, D. Lisak, O.V. Naumenko, L.S. Rothman, H. Tran, N.F. Zobov, J. Buldyreva, C.D. Boone, D. De Vizia, L. Gianfrani, J.-M. Hartmann, R. McPheat, D. Weidmann, J. Murray, N.H. Ngo, O.L. Polyansky, Pure Appl. Chem. **86**(12), 1931–1943 (2014)